

RSC Advances



This is an *Accepted Manuscript*, which has been through the Royal Society of Chemistry peer review process and has been accepted for publication.

Accepted Manuscripts are published online shortly after acceptance, before technical editing, formatting and proof reading. Using this free service, authors can make their results available to the community, in citable form, before we publish the edited article. This *Accepted Manuscript* will be replaced by the edited, formatted and paginated article as soon as this is available.

You can find more information about *Accepted Manuscripts* in the [Information for Authors](#).

Please note that technical editing may introduce minor changes to the text and/or graphics, which may alter content. The journal's standard [Terms & Conditions](#) and the [Ethical guidelines](#) still apply. In no event shall the Royal Society of Chemistry be held responsible for any errors or omissions in this *Accepted Manuscript* or any consequences arising from the use of any information it contains.

ARTICLE

Development of Bovine Serum Albumin–modified Hybrid Nanoclusters for Magnetofluorescent Imaging and Drug Delivery

Cite this: DOI: 10.1039/x0xx00000x

Mochamad Zakki Fahmi,^{†a} Keng-Liang Ou,^{†bcde} Jem-Kun Chen,^f Ming-Hua Ho,^a Shin-Hwa Tzing,^g Jia-Yaw Chang^{a*}Received 00th January 2012,
Accepted 00th January 2012

DOI: 10.1039/x0xx00000x

www.rsc.org/

In this study, bovine serum albumin (BSA) was used for simultaneously clustering and phases-transferring both oil-soluble AgInS₂-ZnS quantum dots (QDs) and MnFe₂O₄ magnetic nanoparticles (MNPs) under ultrasonication. Hybrid nanoclusters, BSA(QMs), thus produced were conjugated with folic acid (FA) and doxorubicin (DOX) to improve their target specificity and drug delivery to HeLa cancer cells. The resulted nanoclusters were characterized by employing different analytical techniques, and the results showed the nanocluster magnetofluorescent property derived from the clustering process. It was also found that the hybrid nanoclusters were biocompatible, non-toxic, and considerably stable over a wide range of pH values and at high ionic strengths. In addition, the *in vitro* confocal microscopy and MR relaxation studies revealed the yellow fluorescence and T₂ contrast-enhancing property of FA-BSA(QMs), as well as their cellular pathway to enter HeLa cells via folate receptor-mediated endocytosis. Furthermore, the cell viability data and flow cytometry results demonstrated the selective uptake of DOX-FA-BSA(QMs) by the HeLa cells, which significantly enhanced cell cytotoxicity. These results suggest that the proposed nanoclusters can be used as an effective and efficient strategy for magnetofluorescent probing and cancer drug delivery.

Introduction

Over the past decades, nanoparticles have been extensively studied for use in various bioimaging, drug targeting, biosensing, and biolabeling applications owing to their unique properties.¹⁻³ In particular, magnetic nanoparticles (MNPs), a highly sensitive nanodevice, has shown great promise for use as a non-invasive contrast agent for biomedical imaging. The modification of MNPs to achieve desired multi-functional property has been intensively investigated.⁴⁻⁶ In most cases, to obtain detailed information at the subcellular level can be challenging for magnetic resonance (MR) technique. Its limited resolution and sensitivity largely degrade the cell specificity of the MR imaging technique and hamper the decision-making on an appropriate treatment strategy. In contrast, semiconductor quantum dots (QDs) exhibit specific band gaps and interesting optical properties like narrow-band emission, emission wavelength tenability, and photostability,⁷⁻⁹ due to their nanosized structures. These properties allow the obtainment of more detailed subcellular information from the diagnostic images. However, the toxicity of QDs is a major drawback, which greatly limits their biological applications. Thus, the development of proper strategies that can eliminate the toxic

effects of QDs without sacrificing their appealing properties is of great importance. Low-toxicity QDs like AgInS₂-ZnS QDs have been developed and widely used as a favorable alternative for generating desired optical images for clinical diagnosis.^{10, 11}

The development of a suitable fabrication strategy for hybrid nanoparticles has become an interesting topic in diverse fields including catalysis,^{12, 13} optoelectronics,^{14, 15} magnetism,¹⁶ and conversion energy.¹⁷ In the biological field, hybrid nanoparticles with combinative structures have also been investigated for producing an efficient imaging system and accurate diagnostic results.¹⁷⁻¹⁹ Among the numerous multifunctional probes, magnetofluorescent nanoparticles that combine QDs and MNPs together show good potential to provide reliable and accurate data for biomedical diagnosis without sacrificing their inherited advantages. Therefore, a large amount of studies have been focused on the synthesis of magnetofluorescent nanoparticles by binding both QDs and MNPs onto high molecular-weight molecules such as synthetic polymers, silica coatings, lipids, and proteins.^{4, 20-22} Although good magnetofluorescent results can be obtained by using those synthesized particles, most approaches are complicated, and the problems caused by the toxicity, instability, and poor biodegradability of the particles still remain unresolved.

In contrast to other types of molecules, proteins are more suitable for developing hybrid nanoparticles for bio-applications, due to their multi-functionality, biocompatibility, stability, and biodegradability. Moreover, the use of proteins can minimize the complexity of the administration process and can reduce the *in vivo* infusion time, making them potent drug nanocarriers for cancer therapy.²³ Among the identified proteins, bovine serum albumin (BSA) is an ideal candidate for fabricating multifunctional nanocarriers. BSA is a zwitterion surfactant with high affinity for binding both hydrophilic compounds and hydrophobic molecules, *e.g.* fatty acids, hematin compounds, and several small aromatic compounds.²⁴⁻²⁶ More importantly, BSA is suitable for use in concentrated salt solutions and can act as carriers for low-water-solubility molecules. As a commercially available protein, BSA is inexpensive and provides various functional groups, through which it can be easily bound with other proteins and peptides,²⁷ as well as synthetic polymers²⁸ and nanoparticles.²⁹ Although the use of BSA for stabilizing single-type nanoparticle and improving the performance of nanocarriers has been reported in several studies,³⁰⁻³² the potential application of BSA as a clustering agent for fabricating hybrid nanoparticles such as magnetofluorescent nanoparticles has been rarely explored.

The previous literatures showed that the synthesis of magnetofluorescent nanoparticles was a complicated process, and that the nanoparticles used for synthesis should be firstly modified as water-soluble particles before being interacted with BSA.³³⁻³⁵ In this study, we developed a direct and simple strategy for preparing hybrid nanoclusters by combining the oil-soluble AgInS₂-ZnS QDs and MnFe₂O₄ nanoparticles together. BSA was applied as a binding agent to simultaneously cluster the nanoparticles and transfer the oil-phase into water-phase nanoclusters. The biocompatibility and cytotoxicity of the resulted BSA(QMs) nanoclusters, as well as their capabilities for magnetofluorescent imaging and drug delivery, were investigated. In addition, the utilization of BSA as a clustering agent and its stability against the variation in pH and ionic strength were also explored in this study. Then, folic acid (FA) was conjugated onto the nanoclusters through chemical reaction; doxorubicin (DOX) cancer drug was associated with the BSA(QMs) nanoclusters via non-covalent interaction to produce the final DOX-FA-BSA(QMs) nanoclusters. The results of *in vitro* transmission electron microscopy (TEM), flow cytometry, confocal laser scanning microscopy (CLSM), and magnetic resonance (MR) imaging analyses demonstrated the potential of using the hybrid nanoclusters for cancer diagnostics and treatment.

Experimental Section

Materials

Zinc stearate (90%), 1-dodecanethiol (DDT, 97%), 1-octadecene (ODE, 90%), potassium ethylxanthate (90%), 3-(4,5-dimethylthiazol-2-yl)-2,5-diphenyltetrazolium bromide (MTT, 97.5%), N-hydroxysulfosuccinimide sodium salt (NHS,

>97%), iron (III) acetylacetonate (Fe(acac)₃, 97%), osmium tetroxide (4%) were purchased from Sigma-Aldrich (Milwaukee, WI, USA). Indium acetate (InAc, 99.98%), silver acetate (AgAc, 99%), glutaraldehyde (25%), Manganese (II) acetylacetonate (Mn(acac)₂, 98%), N,N'-Dicyclohexylcarbodiimide (DCC, 99%) were purchased from Alfa-Aesar (Ward Hill, MA, USA). FA (>98%) was purchased from T.C.I. Chemical Co. (TCI, Japan). Oleylamine (80-90%) and benzyl ether (99%) were purchased from Acros Organics (Geel, Belgium). DOX was purchased from Fusol Material Co., Ltd. (Tainan, Taiwan). Dimethyl sulfoxide (HPLC grade) was purchased from Scharlau (Barcelona, Spain). All chemicals were used directly without further purification.

Synthesis of nanoparticle (AgInS₂-ZnS QDs and MnFe₂O₄ MNP)

The AgInS₂-ZnS QDs were prepared following previously research.¹¹ Firstly, 0.16 mmol of AgAc, 0.29 mmol of InAc, 2.5 mL of DDT and 5 mL of ODE were mixed in a three-neck flask equipped with a condenser, a magnetic stirring bar and a thermometer. The mixture was stirred vigorously under argon flow and subsequently heated to 220°C for 30 min. ZnS precursor was prepared immediately prior to use by mixing zinc stearate (0.79 mmol) in 3 mL of ODE and zinc ethylxanthate (0.097 mmol) in a solvent containing 100 μL of dimethylformamide and 1 mL of toluene, and subsequently added drop-wise to the three-neck flask by a syringe pump (KD Scientific KDS100, USA) at a flow rate of 0.08 mL min⁻¹. After ZnS precursor injection, the reaction mixture was cooled to room temperature and centrifuged at 6000 rpm for 15 min. The precipitate was discarded and the supernatant was then mixed with 5 mL of chloroform. The obtained solution was collected and repeatedly washed with 7.5 mL methanol by centrifugal precipitation. The final product can be dissolved in various nonpolar organic solvents, such as chloroform and toluene.

MnFe₂O₄ MNPs were prepared by mixing 2 mmol of Fe(acac)₃ and 1 mmol of Mn(acac)₂ in the solution of 15 mL benzyl ether and 15 mL oleylamine. The mixture solution was pre-heated to 110°C for 1 h under flow of argon and subsequently heated to 300°C for 1 h. After cooling to the temperature, the resulting mixture was precipitated with ethanol and separated by centrifugation (6000 rpm, 10 min).

Preparation of BSA(QMs)

2.5 mg of QDs and 2.5 mg of MNP were dissolved in chloroform (0.5 mL). Then, the resulting solution was drop-wise added into 10 mL of BSA solution (0.00026 mmol; 20 mg in MES buffer) under ultrasonication (VCX 130 PB, 130 W, 20 kHz, Sonics and Materials Inc., Newton, CT) for 2 min. The cloudy suspension was subsequently centrifuged at 4000 rpm to accelerate the phase separation and separate undesired products. Subsequently, the aqueous solution was extracted and passed through a 0.22 μm nylon filter to remove the aggregated products. The resulting product was denoted as BSA(QMs). For comparison purposes, different samples were obtained by adjusting the weight ratio of BSA and the mixture of QD and

MNP, including 4 : 1, 20 : 1, and 40 : 1, under otherwise identical conditions

Preparation of FA-BSA(QMs) and DOX- FA-BSA(QMs)

NHS-folate was firstly prepared following a previous protocol.³⁶ Briefly, FA (1 g) was dissolved in a mixture of 20 mL of DMSO and 0.5 mL of triethylamine. Following this step, 94 g of DCC and 0.52 g of NHS were added into the reaction system and the mixture was stirred in dark for overnight. The by-product, dicyclohexylurea, was filtered off. NHS-folate was precipitated and washed two times with diethyl ether. After drying in vacuum, a yellow NHS-folate was then dissolved in 1 mL of DMSO and reacted with 10 mL of the above solution containing BSA(QMs) for 24 h. The resulting samples were precipitated by addition of isopropanol and were collected by centrifugation at 4000 rpm (hereafter abbreviated as FA-BSA(QMs)). The collected FA-BSA(QMs) were dispersed in phosphate-buffered saline (PBS, UniRegion Biotech, Taiwan) for the next procedure.

Typical procedures employed for the conjugation of DOX with FA-BSA(QMs) was obtained by mixing DOX (0.25 mg/mL) and FA-BSA(QMs) (4 mg/mL) in 5 mL PBS solution (pH 7.4) and stirred overnight at room temperature in darkness. The unbound DOX in the solution was separated from the FA-BSA(QMs) by a high-flow ultrafiltration membrane (MWCO 50.000 Da; Cellu Sep H1, Orange Scientifique, Belgium) for 24 h. The concentration of DOX was conducted by measuring the absorption of the as-prepared samples at 482 nm against a standard calibration curve. DOX loading efficiency and amount were calculated by the following equation:

$$\text{Loading Efficiency (\%)} = \frac{\text{mass of DOX in BSA(QMs)}}{\text{mass of DOX in feed}} \times 100\% \quad (1)$$

$$\text{Loading Amount(\%)} = \frac{\text{mass of DOX in BSA(QMs)}}{\text{mass of BSA(QMs)}} \times 100\% \quad (2)$$

Cell Culture

In culturing Human cervical (HeLa) cancer cells, Eagle's Minimum Essential Medium (containing 1.5 g/L sodium bicarbonate) supplemented with 1% l-glutamine, 1% antibiotic antimycotic formulation, 1% non-essential amino acid, 1% sodium pyruvate, and 10% fetal bovine serum were used as medium, then the cell was kept in a humidified 5% CO₂ incubator maintained at 37 °C.

Cytotoxicity study

The investigation of cytotoxicity was carried out with MTT assay. HeLa cells were seeded in a 12 well plate at 25,000 cells per well. After 24 h, the cells were washed with PBS and incubated with various concentration of sample for 24 h. After washing twice with PBS, 1 mL of MTT reagent (500 mg mL⁻¹) was then added into the cells. The cells at micro-plate were reincubated for 4 h. After carefully remaining the medium, 200 mL of dimethyl sulfoxide was then added to dissolve the dark-blue formazan crystals. The amount of dark-blue formazan

crystals generated by the live cells was proportional with the number of live cells. The absorbance of dark-blue formazan at 570 nm was measured by using a Biotech Powerwave XS plate reader.

Confocal microscopy scanning imaging

The HeLa cells were firstly seeded in a 6-well plate in 2 mL of culturing medium and cultured for 24 h. After incubating with 300 μL of sample for 60 min, the cells were washed 3 times with PBS solution and then fixed with 70% alcohol for 10 min. Fluorescence images of HeLa cells were acquired by Leica TCS SP2 inverted confocal microscope (Leica Microsystems) equipped with a 63 x 1.32 NA oil immersion objective. Confocal images were obtained by illuminating the samples with the inline Ar (488 nm) and He-Ne (503-680 nm and 588 nm) lasers.

In vitro MR imaging

HeLa cells were seeded into 6-well plates with 2 mL medium and subsequently incubated for 24 h. The medium was replaced with fresh medium (2 mL) containing FA-BSA(QMs) at different concentrations and then incubated for 24 h. After that, the cells were rinsed with PBS, trypsinized, centrifuged, and re-suspended in 1 mL PBS 1.5 mL tubes for MR imaging. T₂ MR imaging was carried out using a Bruker MedSpec 7T with a birdcage head coil.

Bio-TEM observation

The cells were seeded in a 6-well plate in 2 mL of culturing medium and cultured for 24 h then re-incubated for 1 h after addition 300 μL of FA-BSA(QMs). The cells with internalized nanoparticles were trypsinized, centrifuged, and washed with PBS. The resulted cells then fixed with 0.2% glutaraldehyde under 4°C for 5 minutes and two times of 1% glutaraldehyde at 4°C for 60 minutes. Once washed with PBS, the cells were stained with 1 % osmium tetroxide for 60 minutes and washed with PBS. A series of ethanol were further used to dehydrate the cell according to the following procedure: 50%, 70%, 80%, 90%, 95%, and 100% ethanol for 15 min. The epoxy resin, composed from 1 g of cycloaliphatic epoxide resin (ERL 4221); 2.6 g of nonenyl succinic anhydride (NSA); 0.6 g of DER-736 epoxy resin; 0.2 g of 2-(dimethylamino) ethanol (DMAE), was added into the dehydrated cell, then placed in an oven at 60 °C for 48 h. Ultrathin sections of approximately 70 nm thick were cut with diamond knives on Ultramicrotome (Leica Microsystems, Germany) and transferred to 200 mesh copper grids. The images were examined with Philips Tecnai G2 F20 TEM microscope (Philips, Holland).

Flow cytometric analysis

Approximately 3 × 10⁵ cells were separately seeded on cells flask with 5 ml medium for 24 h. The medium was then replaced with 5 mL fresh medium containing different concentration of samples and the cells treated with PBS were used for control. After specific time of incubation, the treated cells were rinsed with PBS, trypsinized, centrifuged, and

suspended in binding buffer. The cells were then stained with 5 μL of Annexin V-FITC for 15 min, washed with binding buffer, and followed by staining with 10 μL of propidium iodide. The samples were analyzed on a Becton Dickinson FACS Calibur flow cytometer equipped with an argon laser (488 nm)

Characterizations

TEM samples were prepared by dropping a dilute solution of nanoparticles onto 200 mesh copper grids coated with a thin Formvar-carbon film and allowing the solvent to evaporate in air at room temperature. High-resolution TEM (HR-TEM) imaging was carried out on a Philips Tecnai G2 F20 microscope (Philips, Holland), equipped with an energy dispersed X-ray spectroscopy (EDS) detector operating at an accelerating voltage of 200 kV. X-ray powder diffraction (XRD) patterns were obtained by using a Rigaku 18 kW rotating anode source X-ray diffractometer with the $\text{Cu K}\alpha_1$ line ($\lambda = 1.54 \text{ \AA}$). UV-vis absorption spectra were measured with a JASCO V-670 spectrometer. Fluorescence spectra were carried out by using a JASCO FP-6500 spectrofluorometer equipped with a 150 W xenon lamp. Magnetic resonance image (MRI) was performed on a Bruker MedSpec 7T whole-body system (Ettlingen, Germany) with a birdcage head coil, to estimate the transverse relaxation time (T_2) for each sample, coronal images (slice thickness = 2 mm) were acquired at various echo times (TE) from 11 to 77 ms with a repetition time (TR) of 5000 ms. The magnetic properties of the nanoparticles were measured by a SQUID magnetometer (Magnetic Property Measurement System 5S, Quantum Design) with maximum applied field up to 10 kOe at room temperature.

Results and Discussion

Synthesis and characterization of nanoparticles

In this study, oil-soluble nanoparticles were chosen due to their well-controlled particle size that simplified the following processes. The hydrocarbon chains from the capping ligands on QDs and MNPs not only contribute to the oil-soluble property of the nanoparticles, but also confine the growth of the nanoparticles with a narrow size distribution. Oil-soluble AgInS_2 -ZnS QDs were prepared in the core/shell system. Firstly, AgInS_2 core QDs were synthesized by using a solvothermal method and then spiked with ZnS precursor in the presence of DDT. The formation of ZnS shell not only enhanced the photoluminescent property of the AgInS_2 core, but also eliminated its intrinsic defects and reduced non-radiative emission. The use of ZnS for enhancing fluorescent intensity was a desirable strategy and particularly investigated in some previous studies.^{10, 11} The synthesized QDs were then characterized by TEM-EDS, and XRD analyses (Fig. S1a-c, Supporting Information). HR-TEM image shown in Fig. S1a confirmed the formation of AgInS_2 -ZnS QDs with diameters

less than 10 nm. TEM inspection at high magnification revealed that the lattice spacing between two adjacent crystal planes of QDs was 3.31 and 3.12 nm, corresponding to the (112) lattice plane of tetragonal AgInS_2 and (111) lattice plane of cubic ZnS, respectively. Elemental characterization by TEM-EDS analysis showed the presence of Ag, In, Zn, and S in the QDs (Fig. S1b). Moreover, XRD pattern of AgInS_2 (JCPDF 75-0117) (Fig. S1c) confirmed the results of HR-TEM analysis, and that the introduction of ZnS precursor into AgInS_2 shifted the initial pattern to a higher degree corresponding to ZnS standard (JCPDF 77-2100).

On the other hand, oil-soluble MnFe_2O_4 MNPs were prepared by using the solvothermal method. The MNPs containing iron and manganese oxide were stabilized by using oleylamine as a capping ligand at a high reaction temperature. Morphological, elemental, and crystal structure analyses were carried out to investigate the formation of MNPs (Fig. 1Sd-e, Supporting Information). HR-TEM analysis identified the spherical nanocrystal of MnFe_2O_4 with d-lattice spacing of 2.13 and 0.57 nm, corresponding to the (004) and (311) lattice planes, respectively (Fig. S1d). In addition, EDS result (Fig. S1e) and conformity XRD pattern (Fig. S1f) confirmed the spinel manganese ferrite structure of MnFe_2O_4 (JCPDF 38-0430).



Scheme 1. Schematic route for preparing DOX-FA-BSA(QMs)

Preparation of BSA(QMs)

To prepare hybrid nanoclusters, we converted the nanoparticle combination and phase transferring processes into a one-step simple procedure by utilizing BSA protein. The phase transferring process for both oil-soluble QDs and MNPs is illustrated in Scheme 1. Empirically, QDs and MNPs were firstly dissolved into chloroform before being mixed with BSA solution. Apart from tryptophan, BSA also contains other amino acids such as proline and histidine acting as a non-polar element.³⁷ It has been reported that the three-dimensional structure of BSA shows large cavities for accommodating non-polar molecules.³⁸

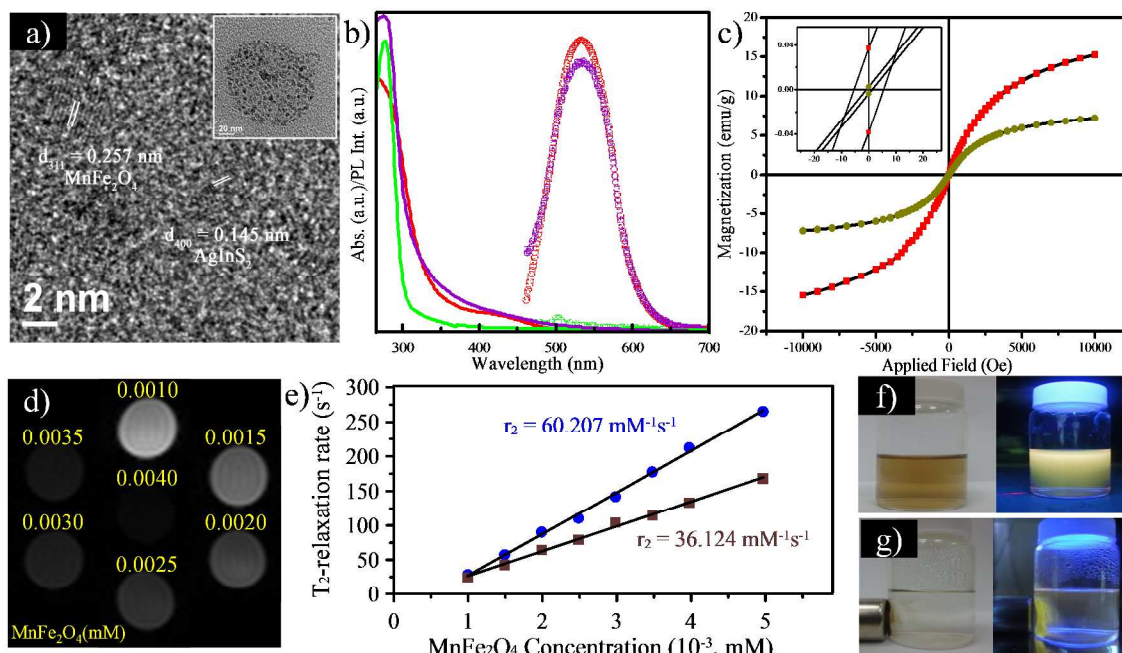


Fig. 1 (a) HR-TEM image of BSA(QMs) showing d-spacing of justified MnFe_2O_4 and $\text{AgInS}_2\text{-ZnS}$, insert: its low magnification image. (b) UV-vis absorption (solid lines) and PL emission spectra (ring lines) of BSA (green), $\text{AgInS}_2\text{-ZnS}$ QDs (red), and BSA(QMs) (purple). (c) Magnetization curves of MnFe_2O_4 (red) and BSA(QMs) (dark yellow), insert graph shows magnetic hysteresis loop at low field region. (d) T_2 -weighted MR image of BSA(QMs) as function of MnFe_2O_4 concentrations (7T, 25°C). (e) T_2 relaxation rate of pristine MnFe_2O_4 (blue dots) and BSA(QMs) (brown dots) as function of MnFe_2O_4 concentration (7T, 25°C). (f) Photograph images of water soluble BSA(QMs) under visible (left) and UV light at 365 nm (right). (g) The continuing figure f on the external magnetic field.

In the present study, the interaction between BSA and the nanoparticles was accelerated by using ultrasound wave, which carried the oil-soluble QDs and MNPs to the appropriate sites on BSA and stimulated the transferring process. It was thought that ultrasonication could also enhance the physical interaction between the nanoparticles and BSA, and that the use of a limited amount of BSA could promote the competition among nanoparticles for interacting with BSA. Consequently, QDs and MNP agglomerated into a cluster surrounded by BSA, resulting in a hybrid nanocluster, BSA(QMs). The formation of BSA(QMs) nanoclusters can intensify the magnetofluorescence without damaging the original structure of each type of nanoparticle.

HR-TEM analysis was performed to preliminarily investigate the structural formation of BSA(QMs) (Fig. 1a). By analyzing the selected image at high magnification, the distance between the adjacent lattice fringes on certain two particles was determined to be 0.257 and 0.18 nm, corresponding to the d-spacing of the lattice plane (311) of MnFe_2O_4 and that of the lattice plane (400) of AgInS_2 , respectively. Moreover, the absorption and emission spectra of BSA(QMs) showed intense adsorption peaks due to pristine BSA and QDs (Fig. 1b). It is well known that the adsorption maximum at 278 nm in UV-vis spectra is due to the $\pi \rightarrow \pi^*$ transition of the aromatic amino acid residues on BSA. The first excitonic absorption on the QDs spectrum coincided with that on the BSA(QMs) spectrum at the same wavelength (around 440 nm), indicating the presence of QDs in BSA(QMs). In addition, signal overlapping

in the PL spectra at $\lambda_{\text{ex}} = 430$ nm also confirmed this finding. The symmetrical emission band at approximately 550 nm was due to QDs instead of BSA. The characteristic adsorption peak of QDs in BSA(QMs) spectra indicated that the clustering process did not damage the structure or optical properties of QDs. In addition, the magnetic properties of pristine MNP and BSA(QMs) were characterized using a SQUID magnetometer at 273 K with the maximum applied field up to 10 kOe. Its hysteresis loops are shown in Fig. 1c. The original saturated magnetization of pristine MNP was 15.26 emu/g and then declined to 7.19 emu/g after the clustering process.

We found that the coating of non-magnetic protein BSA onto the surface of MNPs reduced saturated magnetization, and this finding was consistent with the result of early studies about using BSA to modify MNPs.^{39,40} Magnetic hysteresis was observed in both MNPs and BSA(QMs) with a coercivity value of 8 and 2 kOe, respectively. The insignificant hysteresis and much lower coercivity value than the theoretical value of magnetite (lit.,⁴¹ 92–100 emu/g) indicate the superparamagnetism of the MNPs.

MR imaging with a 7T scanner was performed to explore the feasibility of using the magnetofluorescent nanoclusters as contrast agents (CAs). In a magnetic field, a contrast agent can promote the spin-spin (T_2) or transverse relaxation of adjacent water molecules and affect the intensity of negative signals (*i.e.* signals are shown in darker color). T_2 -weighted MR images showed T_2 relaxation of magnetofluorescent nanoclusters at different concentrations (Fig. 1d). The results indicated that the

sensitivity of the negative signals increased with an increase in nanocluster concentration. Moreover, relaxometric investigation (Fig. 1e) was performed, and T_2 relaxation efficiency (r_2) of pristine MNP and BSA(QMs) was 60.207 and $36.124 \text{ mM}^{-1}\text{s}^{-1}$, respectively. In addition, digital photographs of the clustered BSA(QMs) (Fig. 1f-g), which were obtained under visible and fluorescent lights with or without the use of an external magnetic field, demonstrated the magnetofluorescent property of BSA(QMs).

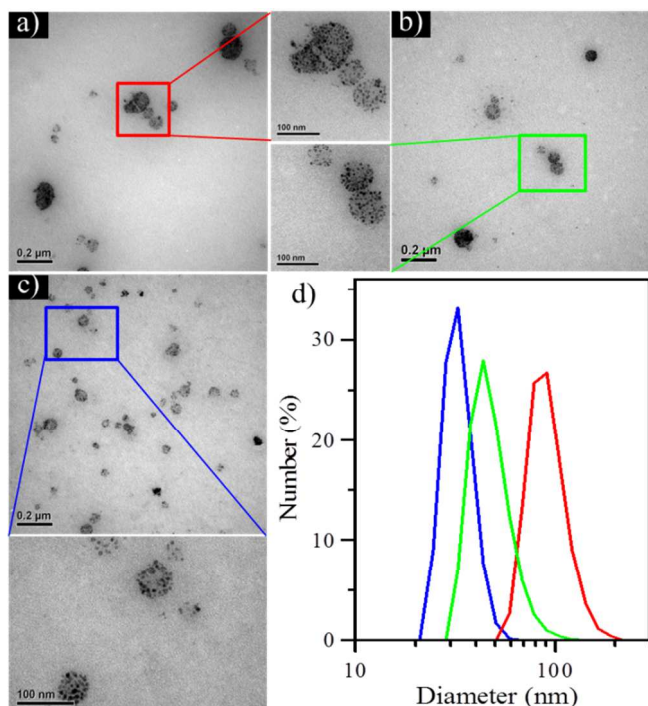


Fig. 2. (a-c) TEM images of BSA(QMs) that vary NPs:BSA ratio to 1:4 (a), 1:20 (b), and 1:40 (c) with its high-magnification images of the adjusted area. (d) Size distribution of NPs:BSA ratio, namely 1:4 (blue), 1:20 (green), and 1:40 (red).

It is reasonable to conclude that BSA plays a key role in the formation of nanoclusters. To investigate the effect of BSA concentration on nanocluster formation, we used different nanoparticles (QDs + MNPs) to BSA weight ratios, 1:4, 1:20, and 1:40, for fabrication and characterized the morphology of the resulted nanoclusters by TEM and dynamic light scattering analyses (Fig. 2). The average size of nanoclusters at nanoparticle/BSA weight ratio of 1:4 was 91.6 nm , and it decreased to 43.82 and 32.67 nm at the weight ratio of 1:20 and 1:40, respectively. The results indicate that small-size nanoclusters can be obtained with the use of high concentration BSA. The nanoparticles are prohibited from clustering with other nanoparticles once being coated with BSA, and the abundant BSA in the reaction solution can prevent the formation of large clusters.

Colloidal stability analysis

Next, we investigated the stability of BSA(QMs) against the variation in pH value and ionic strength. Fig. S2a shows the influence of pH change (from pH 3 to 12) on the stability of

BSA(QMs) nanoclusters. Twenty-four hours after preparation, unstable BSA(QMs) that tended to precipitate were observed at low pH values (pH 3 and vaguely pH 4). The destructed cluster structure of BSA(QMs) at low pH values is related to the conformational change and disrupted molecular interactions of BSA. As reported in the previous literatures,^{42, 43} BSA is present in a compendious shape and shows conformational changes at pH values above 8. The decrease in pH value can enhance the conformation and can expand the BSA structure. The expanded structure of BSA at lower pH values will reduce its ability to maintain the nanocluster structure. In this situation, the electrostatic and hydrophobic interactions between BSA and nanoparticles are significantly disrupted, leading to the collapse of cluster formation. Therefore, precipitation can easily occur under acidic environments. Moreover, the results in Fig. S2b indicated that the formation of nanocluster was independent from the change in ionic strength. The stability of BSA(QMs) at pH 7 was maintained unchanged regardless of the increase in NaCl concentration up to 0.5 M . Unlike the acid effect, the expansion of BSA structure can be prevented in the presence of salt. Furthermore, previous studies showed that a compressed BSA diameter can be achieved in the presence of salt.^{44,45} An increase in ionic strength will promote the hydrophobic interaction between BSA and nanoparticles, resulting in continuous binding between BSA and nanoparticles. These results also suggest that BSA is suitable for use in living organisms due to its excellent stability under various physiological conditions (e.g. blood circulation at pH 7.4, intracellular compartment at pH 5, pancreas region at pH 8.1, and salt concentration 0.15 M).⁴⁶

Conjugation of DOX and FA to BSA(QMs)

As-prepared BSA(QMs) nanoclusters were chemically conjugated with FA for cancer cell targeting by following the procedure described in Scheme 1. In this procedure, DCC and NHS were applied to activate the carboxyl group on FA, produce a reactive intermediate (NHS-Folate), and chemically bond to the amine groups in BSA (especially lysine and arginine amino acid) to form FA-BSA(QMs). Subsequently, DOX was loaded onto BSA via electrostatic interactions. As shown in the previous studies, DOX is positively charged in neutral pH range with acid strength $\text{pK}_a = 8.2$.⁴⁷⁻⁴⁹ Thus, DOX exhibited a high affinity for negatively charged BSA (isoelectric point at $\text{pH} = 5.4$). The conjugation of FA to BSA(QMs) via chemical reaction is important for minimizing the loss of these agents before they reach the target cells; and DOX can be easily released from BSA after being uptaken by cells through physical bonding mechanism. The conjugation of DOX and FA to BSA was confirmed by UV-vis absorption analysis (Fig. 3a). A mound peak at $350\text{-}400 \text{ nm}$ due to $n\text{-}\pi^*$ transitions in the enone region of FA is found in the absorption spectrum of FA-BSA(QMs).⁵⁰ The absorption peak in the DOX-FA-BSA(QMs) spectrum at 485 nm indicates the existence of DOX and in agreement with the previous finding.¹ In addition, the absorption peak at 278 nm is observed from both DOX-FA-BSA(QMs) and FA-BSA(QMs) absorption

spectra, indicating the presence of BSA molecules at the exterior surface of the nanoclusters.

To evaluate the drug delivery potential of the hybrid nanoclusters, we quantitatively determined the loading efficiency and loading amount of DOX on BSA(QMs). Under current experimental condition, the loading efficiency and loading amount was 91.1% and 1.88%, respectively. To achieve the maximum loading capacity, the loading amount of DOX on FA-BSA(QMs) at various DOX concentrations were investigated. The results in Fig. 3b shows that saturated DOX at concentration 175 $\mu\text{g}/\text{mL}$ could be conjugated onto FA-BSA(QMs), and this corresponded to a loading amount of approximately 6%.

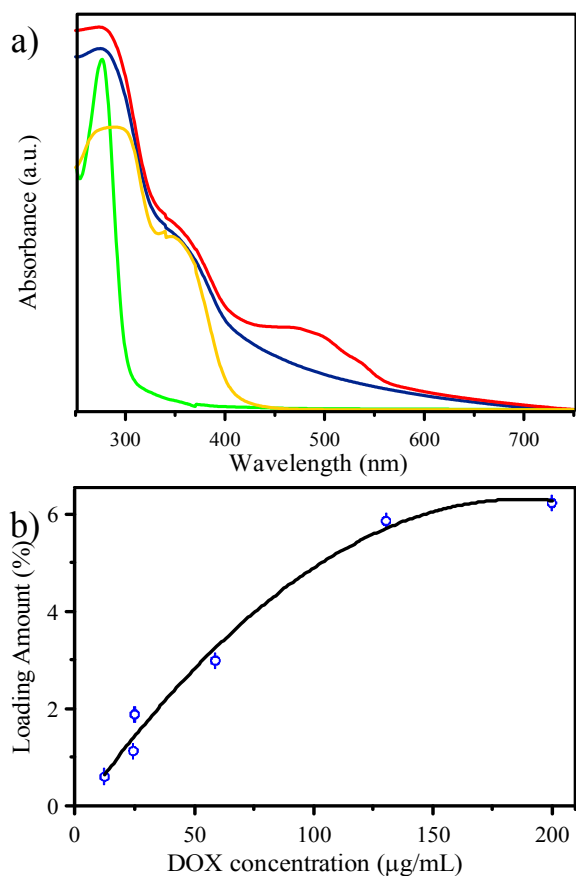


Fig. 3 (a) UV-vis absorption spectra of BSA (green), FA-BSA(QMs) (blue), free FA (yellow), and DOX-FA-BSA(QMs) (red). (b) Loading amount of FA-BSA(QMs) at various DOX concentration (pH solution = 7.4).

Cellular uptake investigation

Cellular uptake efficiency is an important indicator of cell imaging and drug delivery capacity for BSA(QMs). CLSM analysis was performed to examine the internalization of BSA(QMs), FA-BSA(QMs), and DOX-FA-BSA(QMs) into HeLa cancer cells (Fig. 4). By using a laser source at 530 nm, low-intensity yellow fluorescence was observed from BSA(QMs) after incubation for 1 h, indicating the non-specific targeting ability of BSA(QMs) via diffusion through the

endothelium of cancer cells. Intense yellow fluorescence was observed from FA-BSA(QMs), indicating a significant uptake of the nanoclusters by the cells (Fig.3b). As control, we also incubated the HeLa cell with free FA to confirm no disturbing emission from free FA (Fig.S3). This results reveals the effectiveness of using FA to enhance the ability of BSA(QMs) to specifically target cancer cells. Moreover, the confocal microscopic image of FA-BSA(QMs) clearly shows the absence of yellow fluorescence within the nucleus region.

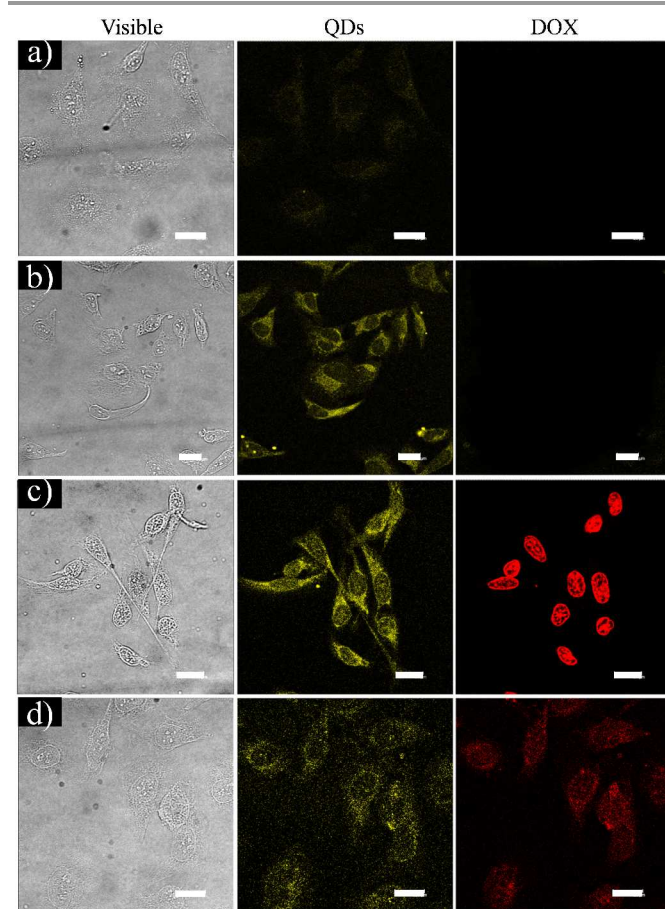


Fig. 4 CLSM images of BSA(QMs) (a), FA-BSA(QMs) (b), DOX-FA-BSA(QMs) (c and d) after 1 h (a-c) and 20 min (d) incubation on HeLa Cells at 37 °C. Scale bars represent 20 μm .

Then, FA-BSA(QMs) were incubated with cells at 4°C for 1 h followed by confocal analysis used for evaluating their ability to accelerate cellular uptake. The confocal image in Fig. S4 clearly shows the existence of nanoclusters in the membranes of the cells. Although all endocytosis processes in cells can be inhibited at low temperatures,⁵¹⁻⁵³ folate-containing materials may possibly reach the cell's membrane by binding through the folate receptor. Thus, yellow fluorescence from BSA(QMs) around the membrane of HeLa cells still remained pronounced. While free DOX cannot significant on reaching HeLa (Fig. S5), the conjugation of DOX onto FA-BSA(QMs) facilitates that and it is indicated by red fluorescence emission from most nuclei of the cells (Fig 4c). Because DOX is a cancer drug that binds with DNA to take effect, the accumulation of DOX in cell

nuclei is a common phenomenon after cellular uptake. To better understand the DOX route of entering the intracellular region, confocal images were captured after HeLa cells were incubated with DOX-FA-BSA(QMs) for 20 min (Fig 4d). The images showed original presence of DOX in the cytoplasm, indicating that the drug was carried and delivered to the cytoplasm before being released from the BSA(QMs) nanoclusters. In general, the intracellular release of DOX is likely to occur under acidic conditions created by the late endosomes (pH 5.5) and by combining the endosome with lysosome (pH 4.5) compartment. In addition, the z-slicing technique performed on CLSM was applied to confirm the presence of FA-BSA(QMs) and DOX-FA-BSA(QMs) in the cytoplasm (Fig. 5). The slicing results showed the yellow fluorescence present only in certain XY planes, indicating that the BSA(QMs) accumulated in the peripheral region of cytoplasm, whereas the released DOX accumulated in the cell nuclei.

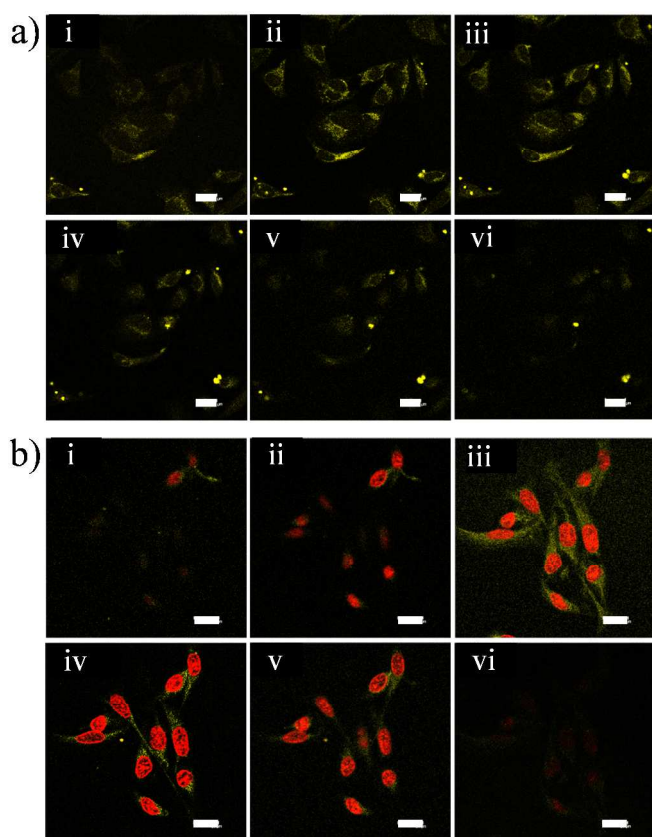


Fig. 5 (a) CLSM images of FA-BSA(QMs) and (b) DOX-FA-BSA(QMs) on z-stack sectioning of HeLa cancer cells from top (i) to bottom (vi) after 1 h incubation. Scale bars represent 20 μm .

Subsequently, *in vitro* T_2 weighted analysis with a 7T MR scanner was conducted to detect the magnetic signal of FA-BSA(QMs) after cellular uptake (Fig. 6a). The T_2 (dark) signal was observed, and the signal was enhanced with the use of high-concentration FA-BSA(QMs), demonstrating the potency of using FA-BSA(QMs) as MR contrast agents. Moreover, TEM analysis of HeLa cells (Fig. 6b) supports the MR result which shows FA-BSA(QMs) can internalize into the cytoplasm

of the cell via endocytosis, in good agreement with our previous findings. In addition, the nanoclusters maintained their original structural formation in the cytoplasm of cell, indicating their high stability under *in vivo* conditions.

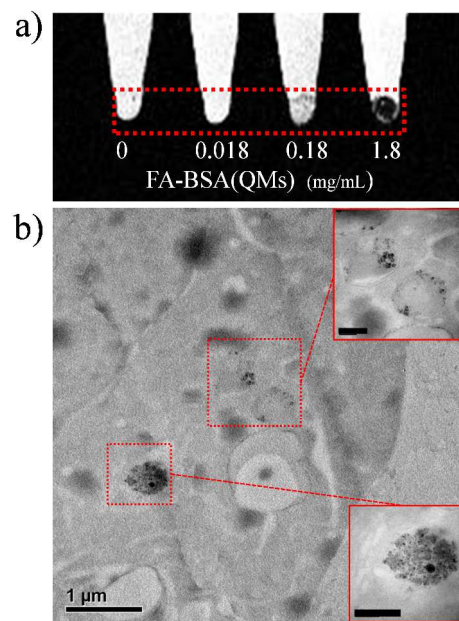


Fig. 6 (a) *In vitro* T_2 -weighted MR image of HeLa cells incubated by specific concentration of FA-BSA(QMs) for 24 h. (b) TEM images show the internalization of FA-BSA(QMs) into HeLa cells, the high-magnification images of signed area delimited by red square with scale bars represent 20 μm .

DOX release and cytotoxicity evaluation

Drug release ability was investigated by dialyzing DOX-FA-BSA(QMs) against water with adjusted pH in a dialysis bag (MWCO 3500). Subsequently, the concentration of released DOX was confirmed by UV-vis absorption analysis. The drug release profile in Fig. 7a indicates that the dissociation of DOX from DOX-FA-BSA(QMs) is a pH-dependent process. A burst release was found in the first 7 h, and the amount of released DOX at pH 5 was consistently higher than at pH 7. However, the release of conjugated DOX seemed to be a slower process controlled by the nanocluster. This phenomenon suggests that a longer release time is required for DOX being interacted with BSA(QMs). In fact, a controllable drug release process is advantageous for therapeutic applications, because it can minimize any possible leakage before the drug reaches the target.⁵⁴ Furthermore, we individually evaluated the cytotoxicity of BSA(QMs), FA-BSA(QMs), and DOX-FA-BSA(QMs) after the incubation with HeLa cells for 24 h. The results in Fig. 7b furnishes that BSA(QMs) and FA-BSA(QMs) exhibited low toxicity against HeLa cells even at the high concentration (400 $\mu\text{g}/\text{mL}$), whereas DOX-FA-BSA(QMs) showed high cytotoxicity at the same concentration. In fact, the cytotoxicity of DOX-FA-BSA(QMs) was relatively low at the low concentration (10 $\mu\text{g}/\text{mL}$); whereas it was significantly increased with an increase in concentration. In addition, we compared the cytotoxicity of DOX-FA-BSA(QMs) and free

DOX at the same DOX concentration under the same conditions loading amount of DOX. The cell viability results presented in Fig. 7c indicates that DOX-FA-BSA(QMs) can significantly reduce the cell viability (IC₅₀ value of approximately 0.705 $\mu\text{g}/\text{mL}$) at high DOX concentrations (above 0.7 $\mu\text{g}/\text{mL}$), as compared with free DOX (IC₅₀ value of 2.35 $\mu\text{g}/\text{mL}$). The presence of FA is considered as main reason for enhanced selective targeting ability and DOX delivery efficiency of the nanoclusters.

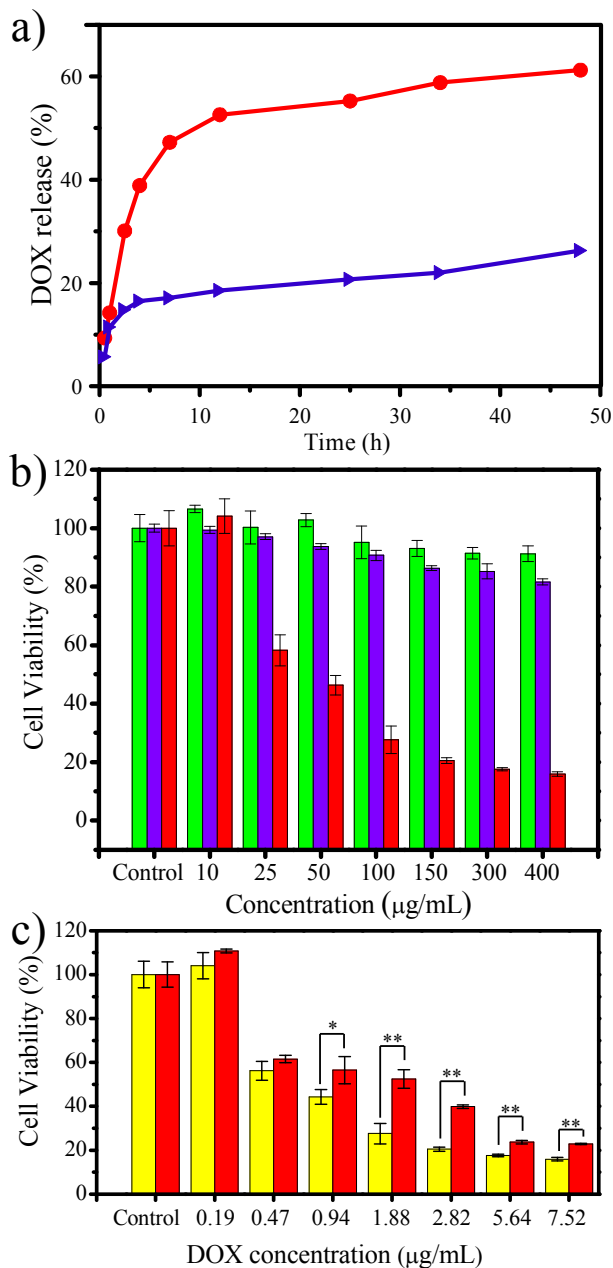


Fig. 7 (a) DOX release profile of DOX-FA-BSA(QMs) on PBS buffer at pH 7.4 (blue) and 5 (red). (b) MTT based cell viability study of HeLa Cells after 24 h treated with BSA(QMs) (green), FA-BSA(QMs) (Violet), and DOX-FA-BSA(QMs) (red). (c) MTT based cell viability study of HeLa Cells after 24 h treated with DOX-FA-BSA(QMs) (yellow) and free DOX (red). All of MTT data are represented as mean \pm SD (n = 3). * $p < 0.05$, ** $p < 0.01$.

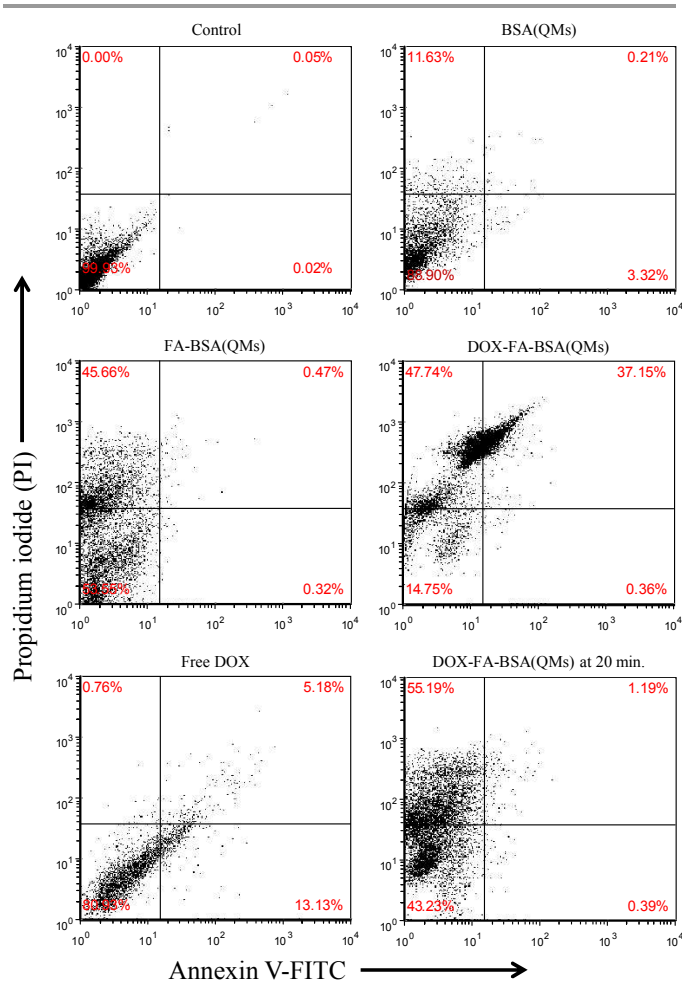


Fig. 8 The apoptosis evaluation of HeLa cells before and after incubated with BSA(QMs), FA-BSA(QMs), free DOX along with DOX-FA-BSA(QMs) for 1 h and first 20 min.

Furthermore, flow cytometry analysis was conducted to determine the number of apoptotic cells caused by BSA(QMs), FA-BSA(QMs), and DOX-FA-BSA(QMs) nanoclusters. This study is important to reveal the toxic effects of these particles on HeLa cells. Annexin V-FITC and propidium iodide were both applied for cell staining. Propidium iodide can reveal cell necrosis via the interaction with DNA and RNA of the cells. Annexin V-FITC shows high affinity for phosphatidylserine, which can be translocated onto the outer layer of the cell membrane during apoptosis.^{55, 56} A 2D plot model was used to present the cell proliferation data collected after the cells were incubated with different types of particles for 1 h (Fig. 8). The results showed insignificant early apoptosis (PI-negative/annexin-positive) and late apoptosis (PI-positive/annexin-positive) of cells after treatment with BSA(QMs) and FA-BSA(QMs), while results in PI-positive/annexin-negative regions refer to cell necrosis. The high-intensity PI signal in the PI-positive region was strongly interfered by the emission of QDs with emission wavelength close to that of PI, and this severely disrupted the detection. Moreover, the percentage shown in PI-positive region can be

used to determine the number of BSA(QMs), and this percentage for FA-BSA(QMs) was higher than that for BSA(QMs), indicating that the use of FA accelerated the internalization of BSA(QMs) into cells. The apoptosis percentage of HeLa cells treated with 10 $\mu\text{g}/\text{mL}$ DOX-FA-BSA(QMs) for 20 min was 1.58%, and this number significantly increased to 37.51% after treatment for 1 h. Moreover, the apoptosis percentage of cells treated with DOX-FA-BSA(QMs) was higher than free DOX (18.31%) under the same condition, agreeing well with the MTT result discussed above. Furthermore, these results demonstrate the effectiveness and efficiency of the hybrid nanocluster strategy for magnetofluorescent probing and cancer drug delivery.

Conclusion

We have demonstrated the application of hybrid BSA(QMs) nanoclusters for magnetofluorescent imaging and drug delivery. The nanoclusters were non-toxic and biocompatible, and exhibited good stability in a wide range of pH values and at high ionic strengths. The strategy for dual-imaging and drug delivery was achieved by conjugating FA and DOX onto the nanoclusters. BSA played an important role in stabilizing the nanoclusters, and its usage suggested the possibility to conjugate additional agents for realizing multi-functionality. An efficient strategy against cancer cells was achieved upon the association of DOX with the nanoclusters. PL emission, confocal microscopy, and magnetic resonance analyses were conducted, and the results clearly showed that the fluorescent and magnetic properties of BSA(QMs) were well retained after the internalization into HeLa cancer cells. Cytotoxicity analysis by MTT and flow cytometry revealed the toxic effect of nanoclusters after binding with DOX. The proposed BSA(QMs) technique can inspire the development of novel approaches for preparing multifunctional nanoparticles for various biological applications.

Acknowledgements

The authors thank the National Science Council of the Republic of China for financially supporting this research under Contract No. NSC 102-2628-M-011-001-M3, and supporting partly by Taipei Medical University under Contract No. TMU102-BIMDPP-02 and TMU102-BIMDPP-04. We thank 7T animal MRI Core Lab of the Neurobiology and Cognitive Science Center, National Taiwan University for technical and facility supports.

Notes and references

- ^a Department of Chemical Engineering, National Taiwan University of Science and Technology, Section 4, #43, Keelung Road, Taipei 106, Taiwan, ROC. Email: jychang@mail.ntust.edu.tw
- ^b Research Center for Biomedical Devices and Prototyping Production, Taipei Medical University, Taipei 110, Taiwan, ROC
- ^c Research Center for Biomedical Implants and Microsurgery Devices, Taipei Medical University, 250 Wu Hsing Street, Taipei 110, Taiwan, ROC
- ^d Department of Biomedical Materials and Tissue Engineering, College of Oral Medicine, Taipei Medical University, 250 Wu Hsing Street, Taipei 110, Taiwan, ROC
- ^e Department of Dentistry, Taipei Medical University-Shuang-Ho Hospital, Taipei 235, Taiwan, ROC

- ^f Department of Materials Science and Engineering, National Taiwan University of Science and Technology, Taipei 106, Taiwan, ROC
- ^g Department of Chemical Engineering, Army Academy, Chung-Li 320, Taiwan, ROC
- † Electronic Supplementary Information (ESI) available: HR-TEM, EDS, XRD, the photograph images of BSA at several pH and NaCl concentration, and additional CLSM. See DOI: 10.1039/b000000x/
- ‡ This authors contributed equally to this work
1. C. Fang, F. M. Kievit, O. Veisoh, Z. R. Stephen, T. Wang, D. Lee, R. G. Ellenbogen and M. Zhang, *J. Control. Release*, 2012, **162**, 233-241.
 2. B. Godin, E. Tasciotti, X. Liu, R. E. Serda and M. Ferrari, *Acc. Chem. Res.*, 2011, **44**, 979-989.
 3. J.-H. Lee, Y.-M. Huh, Y.-W. Jun, J.-W. Seo, J.-T. Jang, H.-T. Song, S. Kim, E.-J. Cho, H.-G. Yoon, J.-S. Suh and J. Cheon, *Nat. Med.*, 2007, **13**, 95-99.
 4. H. M. Kim, H. Lee, K. S. Hong, M. Y. Cho, M.-H. Sung, H. Poo and Y. T. Lim, *ACS Nano*, 2011, **5**, 8230-8240.
 5. H. Lee, S. M. Dellatore, W. M. Miller and P. B. Messersmith, *Science*, 2007, **318**, 426-430.
 6. B. Qi, L. Ye, R. Stone, C. Dennis, T. M. Crawford and O. T. Mefford, *J. Phys. Chem. C*, 2013, **117**, 5429-5435.
 7. X. Yang, D. Zhao, K. S. Leck, S. T. Tan, Y. X. Tang, J. Zhao, H. V. Demir and X. W. Sun, *Adv. Mater.*, 2012, **24**, 4180-4185.
 8. S. Kim, B. Fisher, H.-J. Eisler and M. Bawendi, *J. Am. Chem. Soc.*, 2003, **125**, 11466-11467.
 9. U. Resch-Genger, M. Grabolle, S. Cavaliere-Jaricot, R. Nitschke and T. Nann, *Nat. Meth.*, 2008, **5**, 763-775.
 10. J.-Y. Chang, G.-Q. Wang, C.-Y. Cheng, W.-X. Lin and J.-C. Hsu, *J. Mater. Chem.*, 2012, **22**, 10609-10618.
 11. M. Z. Fahmi and J.-Y. Chang, *Nanoscale*, 2013, **5**, 1517-1528.
 12. X. Sun, Y. Zhang, P. Song, J. Pan, L. Zhuang, W. Xu and W. Xing, *ACS Catalysis*, 2013, **3**, 1726-1729.
 13. R. Bhandari, D. B. Pacardo, N. M. Bedford, R. R. Naik and M. R. Knecht, *J. Phys. Chem. C*, 2013, **117**, 18053-18062.
 14. R. O'Hayre, M. Nanu, J. Schoonman, A. Goossens, Q. Wang and M. Grätzel, *Adv. Funct. Mater.*, 2006, **16**, 1566-1576.
 15. T. Mokari, E. Rothenberg, I. Popov, R. Costi and U. Banin, *Science*, 2004, **304**, 1787-1790.
 16. Y. Yu, K. Sun, Y. Tian, X. Z. Li, M. J. Kramer, D. J. Sellmyer, J. E. Shield and S. Sun, *Nano Lett.*, 2013, **13**, 4975-4979.
 17. R. Costi, A. E. Saunders, E. Elmalem, A. Salant and U. Banin, *Nano Lett.*, 2008, **8**, 637-641.
 18. J.-S. Choi, J. C. Park, H. Nah, S. Woo, J. Oh, K. M. Kim, G. J. Cheon, Y. Chang, J. Yoo and J. Cheon, *Angew. Chem. Int. Ed.*, 2008, **47**, 6259-6262.
 19. J. Chen, Z. Guo, H.-B. Wang, M. Gong, X.-K. Kong, P. Xia and Q.-W. Chen, *Biomaterials*, 2013, **34**, 571-581.
 20. F. Erogobgo, K.-T. Yong, R. Hu, W.-C. Law, H. Ding, C.-W. Chang, P. N. Prasad and M. T. Swihart, *ACS Nano*, 2010, **4**, 5131-5138.
 21. J.-H. Park, G. von Maltzahn, E. Ruoslahti, S. N. Bhatia and M. J. Sailor, *Angew. Chem. Int. Ed.*, 2008, **120**, 7394-7398.
 22. A. Scheffold, S. Miltenyi and A. Radbruch, *Immunotechnology*, 1995, **1**, 127-137.
 23. M. J. Hawkins, P. Soon-Shiong and N. Desai, *Adv. Drug Deliver. Rev.*, 2008, **60**, 876-885.

24. R. Brodersen, *J. Biol. Chem.*, 1979, **254**, 2364-2369.
25. J. E. Fletcher, A. A. Spector and J. D. Ashbrook, *Biochemistry*, 1971, **10**, 3229-3232.
26. A. Mallick, S. C. Bera, S. Maiti and N. Chattopadhyay, *Biophys. Chem.*, 2004, **112**, 9-14.
27. A. Angelini, J. Morales-Sanfrutos, P. Diderich, S. Chen and C. Heinis, *J. Med. Chem.*, 2012, **55**, 10187-10197.
28. C. He, J. Liu, L. Xie, Q. Zhang, C. Li, D. Gui, G. Zhang and C. Wu, *Langmuir*, 2009, **25**, 13456-13460.
29. B. Zhang, X. Wang, F. Liu, Y. Cheng and D. Shi, *Langmuir*, 2012, **28**, 16605-16613.
30. P. Murawala, A. Tirmale, A. Shiras and B. L. V. Prasad, *Mater. Sci. Eng. C*, 2014, **34**, 158-167.
31. J.-H. Lee, K. Lee, S. H. Moon, Y. Lee, T. G. Park and J. Cheon, *Angew. Chem.*, 2009, **121**, 4238-4243.
32. P. Kocbek, N. Obermajer, M. Cegnar, J. Kos and J. Kristl, *J. Control. Release*, 2007, **120**, 18-26.
33. J. Wu, Z. Ye, G. Wang and J. Yuan, *Talanta*, 2007, **72**, 1693-1697.
34. F. Mahtab, Y. Yu, J. W. Y. Lam, J. Liu, B. Zhang, P. Lu, X. Zhang and B. Z. Tang, *Adv. Funct. Mater.*, 2011, **21**, 1733-1740.
35. P. Sun, H. Zhang, C. Liu, J. Fang, M. Wang, J. Chen, J. Zhang, C. Mao and S. Xu, *Langmuir*, 2009, **26**, 1278-1284.
36. L. Zhang, S. Hou, S. Mao, D. Wei, X. Song and Y. Lu, *Int. J. Pharm.*, 2004, **287**, 155-162.
37. S. Soares, N. Mateus and V. de Freitas, *J. Agric. Food. Chem.*, 2007, **55**, 6726-6735.
38. B. Huang, H.-Y. Kim and C. Dass, *J. Am. Soc. Mass. Spectrom.*, 2004, **15**, 1237-1247.
39. L. Liu, Y. Ma, X. Chen, X. Xiong and S. Shi, *J. Chromatogr. B*, 2012, **887-888**, 55-60.
40. B. Zhang, Q. Li, P. Yin, Y. Rui, Y. Qiu, Y. Wang and D. Shi, *ACS Appl. Mater. Interfaces*, 2012, **4**, 6479-6486.
41. R. Sondjaja, T. Alan Hatton and M. K. C. Tam, *J. Magn. Magn. Mater.*, 2009, **321**, 2393-2397.
42. E. Edri and O. Regev, *Anal. Chem.*, 2008, **80**, 4049-4054.
43. V. R. Zurawski and J. F. Foster, *Biochemistry*, 1974, **13**, 3465-3471.
44. D. Gao, D.-Q. Lin and S.-J. Yao, *J. Chromatogr. B*, 2007, **859**, 16-23.
45. R. E. Martenson, *J. Biol. Chem.*, 1978, **253**, 8887-8893.
46. D. Schmaljohann, *Adv. Drug Deliver. Rev.*, 2006, **58**, 1655-1670.
47. H. Hao, Q. Ma, C. Huang, F. He and P. Yao, *Int. J. Pharm.*, 2013, **444**, 77-84.
48. J. Qi, P. Yao, F. He, C. Yu and C. Huang, *Int. J. Pharm.*, 2010, **393**, 177-185.
49. C. Tan, Z. Sun, Y. Hong, Y. Li, X. Chen and X. Zhang, *J. Mater. Chem. B*, 2013, **1**, 3694.
50. B. Sahoo, K. S. P. Devi, S. K. Sahu, S. Nayak, T. K. Maiti, D. Dhara and P. Pramanik, *Biomater. Sci.*, 2013, **1**, 647-657.
51. R. J. Lee and P. S. Low, *J. Biol. Chem.*, 1994, **269**, 3198-3204.
52. C. P. Leamon and P. S. Low, *P. Natl. Acad. Sci.*, 1991, **88**, 5572-5576.
53. C. He, Y. Hu, L. Yin, C. Tang and C. Yin, *Biomaterials*, 2010, **31**, 3657-3666.
54. I. I. Slowing, J. L. Vivero-Escoto, C.-W. Wu and V. S. Y. Lin, *Adv. Drug Deliver. Rev.*, 2008, **60**, 1278-1288.
55. M. Vitale, L. Zamai, G. Mazzotti, A. Cataldi and E. Falcieri, *Histochemistry*, 1993, **100**, 223-229.
56. I. Vermes, C. Haanen, H. Steffens-Nakken and C. Reutellingsperger, *J. Immunol. Methods*, 1995, **184**, 39-51.